Title

Generalized Lyzenga's Predictor of Shallow Water Depth for Multispectral Satellite Imagery

Running Head

Generalized predictor of shallow water depth

Author names

Ariyo Kanno[1], Yoji Tanaka[2], Akira Kurosawa[3], and Masahiko Sekine[4]

Affiliations

1. Graduate School of Science and Engineering, Yamaguchi University
2. Graduate School of Urban Innovation, Yokohama National University
3. Location Intelligence System Department, Hitachi Solutions, Ltd
4. Graduate School of Science and Engineering, Yamaguchi University

Mailing addresses

1. 2-16-1 Tokiwadai, Ube, Yamaguchi 755-8611, Japan
2. 79-5 Tokiwadai, Hodogayaku, Yokohama 240-8501, Japan
3. 4-12-7, Higashishinagawa, Shinagawa-ku, Tokyo, 140-0002, Japan
4. 2-16-1 Tokiwadai, Ube, Yamaguchi 755-8611, Japan

Phone numbers

1. +81-836-31-3105
2. +81-45-339-4035
3. +81-3-5780-2111
4. +81-836-85-9311

Fax numbers

1. +81-836-31-3105
2. +81-45-339-4035
3. +81-3-5780-2167
4. +81-836-85-9301

Email addresses

1. kanno@yamaguchi-u.ac.jp

2. tanaka-yo@ynu.ac.jp
3. akira.kurosawa.rr@hitachi-solutions.com
4. ms@yamaguchi-u.ac.jp

Abstract

Multispectral satellite remote sensing can predict shallow-water depth distribution inexpensively and exhaustively, but it requires many in-situ measurements for calibration. To extend its feasibility, we improved and employed a recently developed technique, for the first time, to obtain a generalized predictor of depth. We used six WorldView-2 images and obtained a predictor that yielded a 0.648 m root-mean-square error against a dataset with a 5.544 m standard deviation of depth. The predictor can be used with as few as two pixels with known depth per image, or with no depth data whatsoever, if only relative depth is needed. (98 words)

Subject terms

Bathymetry, multispectral, satellite remote sensing, coral reef

Main Text

I. INTRODUCTION

Bathymetric mapping is fundamental to the study and management of coastal zones and watersheds because water depth distribution governs the physical and biological characteristics (e.g., flows, waves, and benthic habitats) of those areas. However, in shallow and rugged areas such as coral reefs, there is no perfect method for exhaustive bathymetric mapping. Conventional ship sounding is time consuming and constrained by ship access, while use of Airborne LIght Detection And Ranging (LIDAR) for bathymetry is costly.

To supplement these approaches, a number of passive remote sensing methods, using multispectral (Spitzer and Dirks 1987; Stumpf *et al.* 2003; Leckie *et al.* 2005; Lyzenga *et al.* 2006; Daniell 2008; Ribeiro *et al.* 2008; Su *et al.* 2008; Bramante et al. 2013) or hyperspectral (Lee *et al.* 1999; Mobley *et al.* 2005) imagery, have been proposed. These methods are based on the fact that the in-water volume scattering and bottom reflection components of the observed visible radiance depend on water depth. Among these methods, those requiring only one multispectral satellite image and some depth measurements can be applied quickly and inexpensively. The latest multispectral satellite sensors, operating at very high resolution (around 2 m), are especially suited for capturing coral reefs with complex structure.

Among these remote sensing methods, there is a widely applied method known as Lyzenga's method (Clark *et al.* 1990; Winterbottom and Gilvear 1997; Bryant and Gilvear 1999; Feurer *et al.* 2008; Hogrefe *et al.* 2008; Flener *et al.* 2012). This method (fully documented by Lyzenga *et al.* (2006) but originally proposed by others (Paredes and Spero 1983; Lyzenga 1985; Clark *et al.* 1987)) consists of a regression using a physically based predictor of water depth. It uses a number of pixels with known (i.e. measured in-situ) depth as training data and then estimates the coefficients of the predictor, which is a linear function

of image-derived variables for each visible band. The predictor then calculates the water depth of other pixels with unknown depths.

Theoretically, the optimal coefficients of the predictor will depend on the optical conditions of the target image: the bottom surface types, the in-water attenuation coefficient, the state of the atmosphere and water surface, and the elevations of the sun and the satellite sensor. Though use of multiple visible bands can reduce the effect of variations in bottom surface on the predicted depth (Lyzenga *et al.* 2006; Kanno and Tanaka 2012), predictor coefficients are usually estimated independently for each target image. Obviously, such independent estimations require a number of pixels with known depth in each image.

To address this limitation, Kanno and Tanaka (2012) have recently proposed a technique, using pixels of known depth in multiple images obtained by the same sensor, to estimate more generalized coefficients. The coefficients estimated by this technique are not greatly affected by the state of the atmosphere and water surface or by the elevations of the sun and the satellite sensor. It is hoped that once this general set of coefficients is estimated, it can be reliably applied to other images, collected at various times and locations using the same sensor, without requiring a number of pixels with known depth for the calibration for each image. This generalization would thus save the effort for in-situ depth measurement and improve the feasibility of Lyzenga's method. Unfortunately, the technique has not been extensively tested, and the set of generalized coefficients has not yet been presented.

In this study, we apply the technique proposed by Kanno and Tanaka (2012) to a dataset composed of six WorldView-2 images of coral reefs and corresponding depth measurements. We then construct, for the first time, a set of generalized coefficients for application to other shallow-water images. To improve the generality of the coefficients in terms of water quality, we also propose and apply an additional generalization technique that partially corrects for the differences in in-water attenuation coefficients among the target images.

WorldView-2 imagery was selected because of its six visible bands, the greatest number available in current high-resolution satellite imaging. Since the robustness of the predictor against variations in bottom surface type increases with the number of visible bands used (Lyzenga *et al.* 2006; Kanno and Tanaka 2012), our selection of WorldView-2 imagery should yield the greatest generality.

II. LYZENGA'S METHOD

Lyzenga's method (Lyzenga *et al.* 2006) is based on a simple radiative transfer model for shallow water. In this model, the top-of-atmosphere spectral radiance, L_i [$W \cdot m^{-2} \cdot sr^{-1} \cdot \mu m^{-1}$], for the i th visible band of a shallow water pixel is considered as the sum of two components: the spectral radiance which would be observed if the pixel had an infinite water depth ($L_{i,\infty}$), and an exponential function of water depth. After $L_{i,\infty}$ is approximated by using the spectral radiances observed for deep-water pixels and for near-infrared bands, the method calculates a variable $X_i \equiv \log\left[L_i - L_{i,\infty}\right]$, which is expected to be linearly related to water depth h as

$$X_i = -k_i h + C_i. \tag{1}$$

Here, k_i is the in-water effective attenuation coefficient of the i th band and C_i is a term dependent on the bottom reflectance, apparent reflectance of deep water due to in-water scattering, round-trip transmittance through the atmosphere and water surface, and downwelling irradiance at the top of the atmosphere, for the i th band.

After X_i is calculated for all M visible bands used $(i = 1, \cdots, M)$, h for each target pixel is calculated by the following predictor:

$$h = \beta_0 + \beta_1 X_1 + \cdots + \beta_M X_M. \tag{2}$$

Here, $\beta_0, \beta_1, \cdots, \beta_M$ are coefficients estimated by the least-squares method (Gentle, 1998) using pixels with known depth.If we substitute (1) into (2), we get

$$h = \left(-\sum_{i=1}^{M} \beta_i k_i \right) h + \left(\beta_0 + \sum_{i=1}^{M} C_i \beta_i \right) \tag{3}$$

which means that the following conditions:

$$\begin{cases} \sum_{i=1}^{M} \beta_i k_i = -1 \\ \beta_0 + \sum_{i=1}^{M} C_i \beta_i = 0 \end{cases} \tag{4}$$

are required for (2) to be physically based.

In order to account for the effect of the sun and satellite elevations on the in-water optical path length, Lyzenga *et al*. (2006) modeled the effective attenuation coefficient $k_i (i = 1, \cdots, M)$ as

$$k_i = \kappa_i (\sec\theta_S + \sec\theta_V). \tag{5}$$

Here, θ_S is the solar zenith angle and θ_V is the nadir view angle below the water surface; κ_i is the k_i value at $\theta_S = \theta_V = 0$ (when both the sun and the satellite are at the zenith). Although not shown by Lyzenga *et al*. (2006), this modeling corresponds to changing (2) into

$$h = \beta_0 + \beta_1 X_1' + \cdots + \beta_M X_M' \tag{6}$$

where $X_i' \equiv X_i / (\sec\theta_S + \sec\theta_V)$ for $i = 1, \cdots, M$. Note that this modification does not account for the effect of the sun and satellite elevations on the optical path length in the atmosphere.

III. GENERALIZATION TECHNIQUE PROPOSED BY KANNO AND TANAKA

Lyzenga *et al*. (2006) tried to obtain coefficients $\beta_0, \beta_1, \cdots, \beta_M$ with some generality using pixels with known depth from various images as training data. However, this simple approach did not take into

account that C_i in (1) varies among images, depending on the elevations of the sun and the satellite sensor (the optical path length in the atmosphere) and on the states of the atmosphere and water surface. The differences in these above-surface optical conditions among the images will degrade the generality of the estimated coefficients in terms of the bottom surface type. Kanno and Tanaka (2012) pointed out this problem and showed that the effect of the differences can be absorbed by β_0 if we optimize β_0 for each target image. This corresponds to modifying (6) as

$$h = \beta_{0,n} + \beta_1 X_1' + \cdots + \beta_M X_M' \tag{7}$$

where $\beta_{0,n}$ is the β_0 value for the n th ($n = 1, \cdots, N$; N being the number of images used) image.

The coefficients $\beta_1, \cdots, \beta_M$ and $\beta_{0,1}, \cdots, \beta_{0,N}$ for predictor (7) can be estimated by applying the least-squares fitting of the linear model

$$h = (\gamma_1, \cdots, \gamma_N, X_1', \cdots, X_M')(\beta_{0,1}, \cdots, \beta_{0,N}, \beta_1, \cdots, \beta_M)^T \tag{8}$$

to the pixels with known depth. Here, $\gamma_n (n = 1, \cdots, N)$ is a variable that equals 1 for the n th image and 0 for the others, and the superscript *T* indicates transpose.

Theoretically, the coefficients $\beta_1, \cdots, \beta_M$ estimated by this technique are not affected by variations in the above-surface optical conditions among images—i.e., the elevations of the sun and the satellite sensor, and the states of the atmosphere and water surface. They should therefore be more generally applicable than the coefficients estimated by Lyzenga's method using the same set of pixels with known depth. When applying predictor (7) using our estimated coefficients ($\beta_1, \cdots, \beta_M$) to other images, only $\beta_{0,n}$ (β_0 for each image) remains to be calculated. To calculate β_0 for a given image, we require a minimum of just one pixel with known depth.

IV. ADDITIONAL GENERALIZATION TECHNIQUE

The generalization technique proposed by Kanno and Tanaka (2012) adjusts the offset (β_0) of the predictor for each target image. As described above, this technique corrects for variations in the above-surface optical conditions but not for variations in the in-water attenuation coefficients $\kappa_i (i = 1, \cdots, M)$ among images. To make the estimated coefficients ($\beta_1, \cdots, \beta_M$) applicable to images with different κ_i values, further adjustment according to (4) is needed.

For example, suppose a case when the κ_i value for target image A is α times that for target image B for each band. Based on (4) and (5), $\beta_1, \cdots, \beta_M$ for image A must be set at $1/\alpha$ times those for image B. This is achieved by adjusting not only the offset (β_0) but also the gain of the predictor: multiplying predictor (7) by an image-specific factor for each image. In general expression, the gain adjustment corresponds to modifying (7) as

$$h = p_n \left(\beta_{0,n} + \beta_1 X_1' + \cdots + \beta_M X_M' \right) \tag{9}$$

where $p_n (n = 1, \cdots, N)$ is the factor for the n th image and $p_1 = 1$. In order to estimate the coefficients for this model, the least-squares fitting of the following linear model should be repeated, adjusting $p_n (n = 2, \cdots, N)$ using a nonlinear optimization method to minimize the residual sum of squares. In the application described in Section V, $p_n (n = 2, \cdots, N)$ was optimized using the method proposed by Nelder and Mead (1965).

$$h = p_n (\gamma_1, \cdots, \gamma_N, X_1', \cdots, X_M') (\beta_{0,1}, \cdots, \beta_{0,N}, \beta_1, \cdots, \beta_M)^T \tag{10}$$

Obviously, the additional "gain adjustment" technique proposed here cannot perfectly correct for the variation in κ_i when the ratio of κ_i between any two of the target images depends on band i. Still, the technique should make the estimated coefficients $\beta_1, \cdots, \beta_M$ more accurately applicable to images with

different κ_i values than those proposed by Kanno and Tanaka (2012). All that is needed for applying predictor (9) with the estimated coefficients to other images is the remaining coefficient ($\beta_{0,n}$) and the gain (p_n), both of which can be calculated based on a minimum of two pixels of known depth.

V. APPLICATION

A. Datasets and Procedure

The generalization techniques described in III and IV were applied to six WorldView-2 images of shallow water areas and the corresponding depth soundings. The images used, which are shown in Fig. 1, were standard multispectral image products of WorldView-2, with a pixel size of 2×2 m^2. Depth measurement data were collected using a shipboard Acoustic Doppler Current Profiler (RD Instruments, Workhorse Sentinel ADCP) for images 1 and 2 and fishfinders (EAGLE GPS and Lowrance HDS-5) for images 3–5. For image 6, depth measurements using a multi-narrow-beam echo sounder (Reson SeaBat 7125) were provided by the U.S. Naval Oceanographic Office via the website of the National Oceanic & Atmospheric Administration (NOAA)'s National Geophysical Data Center. In all surveys, positioning data were collected using differential GPS.

The pixels with known depth were prepared as follows. First, all depth measurement data were corrected for tide level, so that the data represented the depth values at the time of image acquisition. Next, the pixels with multiple depth measurements were specified by a spatial overlay of each satellite image with depth measurement points. The pixels with small variation coefficients in the depth measurements were then designated as pixels with known depth. The “measured depth” for each of these pixels was defined as the average of its depth measurements. The specifications of each image and the corresponding pixels with known depth are listed in Table 1. The depth statistics of the pixels with known depth for each

image are shown in Table 2.

The numbers of pixels with known depth differed greatly among the target images (Table 1). In order to equalize the contribution of each image, the weighted least-squares method (Gentle 1998) was used instead of the ordinary least-squares method in fitting the model ((8) or (10)) to the pixels with known depth. Here, the relative weight for the pixels in each image was set as the inverse of the number of pixels with known depth in the image. The same weight was applied in calculating the essential statistics for all six images: the mean and Standard Deviation (SD) of the water depth of the pixels with known depth, the Root Mean Square of Residuals (RMSR), and the Root Mean Square Error of predictions (RMSE).

The RMSR and RMSE are the error statistics used to evaluate the goodness of fit and the prediction accuracy of the models, respectively. The RMSR for all six images is defined as

$$RMSR = \sqrt{\frac{\sum_{pixel \in V} w_n (h_O - h_P)^2}{\sum_{pixel \in V} w_n}}. \tag{11}$$

Here, w_n is the relative weight for each pixel, h_O is the measured depth, and h_P is the depth (h) evaluated by predictor (7) or (9) using the estimated coefficients (fitted depth). V is the set of pixels with known depth to which model (8) or (10) is fitted (training data); this set is, in fact, a set of all of the pixels with known depth in our study (6221 in total). The discrepancy between the measured and fitted depths, $h_O - h_P$, is called residual, and the RMSR is a measure of the overall magnitude of the residuals in meters. The closer the RMSR to zero, the better is the model fit. The RMSR for a single image can also be defined as (11), but in this case, V only includes the training data pixels that belong to the image of interest, resulting in the weight being constant and not effective.

The RMSE is similarly defined except that V is not the training data but a different set of pixels used to evaluate the prediction accuracy of the model (test data). Thus, in case of RMSE, h_P is not called “fitted

depth" but "predicted depth" and $h_O - h_P$ is not called "residual" but "prediction error." The RMSE is a measure of the overall magnitude of the prediction errors in meters. The closer the RMSE to zero, the better is the prediction accuracy of the model.

Because the calculation of the RMSE requires test data as well as training data, we randomly selected 622 (10%) of the pixels with known depth as the test data and used the rest (90%) as the training data. We repeated the trial (the random division of the pixels with known depth into training and test data, the estimation of the predictor coefficients using the training data, and the prediction of the test data using the estimated coefficients) 1000 times and calculated RMSE using the virtual test data consisting of 622000 pixels with known depth. This method, referred to as cross validation (Hastie et al. 2001), yields more stable values of the RMSE than a single trial.

B. Results and Discussion

Fig. 2 is a scattergram of fitted depth against measured depth for the fitting of the linear model (8) (to estimate the coefficients of Kanno and Tanaka (2012)'s predictor (7) described in III, which is different from Lyzenga's predictor (6) in that the offset term is adjusted for each target image) to the pixels with known depth from the six images. Fig. 3 is the scattergram of fitted depth against measured depth for the fitting of linear model (10) (to estimate the coefficients of predictor (9) proposed in IV, which is different from predictor (7) in that the gain of the predictor as well as the offset is adjusted for each target image). Table 2 lists the RMSR and RMSE values of these fits, for all six images together and for each individual image.

The overall distribution of the points shown in Fig. 2(a) and Fig. 3(a) is largely along the line y = x shown in red, indicating good overall fittings. However, if we look into the result for the individual images in Fig. 2, the distribution of points is not along the line y = x for some images. For images 2 and 3, the fitted depth tends to be too large for relatively small depths and too small for relatively large depths. In

other terms, the points of images 2 and 3 are distributed nearly horizontally in Fig. 2(b). Further, for image 4, we cannot even observe a positive correlation between the measured and fitted depths. In fact, the correlation coefficient was negative (-0.154) for the image. On the other hand, image 1 may have the opposite problem: underestimation for relatively small depths and overestimation for relatively large depths. These problems indicate that the offset-adjustment technique proposed by Kanno and Tanaka (2012) (described in III) could not sufficiently generalize the predictor.

A possible reason for this failure is the difference in the in-water attenuation coefficient $\kappa_i (i = 1, \cdots, M)$ among images. In general, the clarity of the water is inversely proportional to the response of the observed radiance (or the variable X_i' derived from the observed radiance) to the water depth. Therefore, if images 2 and 3 have smaller attenuation coefficients compared to the other images, then, the coefficients $\beta_1, \cdots, \beta_M$ of predictor (7) (or the corresponding model (8)) for the images should ideally be larger in magnitude. However, because the coefficients are common to all the images, the least-squares fitting just yields "compromise" coefficients, which might be appropriate for some images but too small for images 2 and 3.

The problems found in Fig. 2 seem to be less significant in Fig. 3, which shows fitted depth plotted against measured depth for the linear model (10) including the new gain adjustment, indicating that they were mitigated by the additional gain adjustment. This is confirmed in Table 2 by the fact that, for each of images 2, 3 and 4, the RMSR decreases by the addition of the gain adjustment by no less than 29.4%. Actually, the RMSR for each of the six images decreases by more than 8.3%, resulting in an overall decrease of 28.8%. The largest decrease is 71.8%, for image 1. The decrease ratio corresponds to 0.866 m in absolute value, exceeding 40% of the mean depth (2.143 m) and 210% of the SD of depth (0.411 m). Although not shown in Table 2, the correlation coefficient between the measured and fitted depths for image 4 turned positive (0.348) by the addition of the gain adjustment. The correlation coefficient was

much higher for the other five images (0.562–0.928). Thus, the gain adjustment in addition to the offset adjustment significantly improves the fitting.

Furthermore, as shown in Table 2, the RMSE of prediction similarly decreased with the gain adjustment. In fact, the RMSE values shown in Table 2 are close to the corresponding RMSR values: The maximum difference between the RMSR and RMSE values is just 0.026 m in absolute value and 4.7% in ratio. Thus, a discussion similar to the one above applies to RMSE. The RMSE for each of the six images decreases by more than 8.5% as a result of the additional gain adjustment. The overall RMSE for the six images (mean depth: 3.270 m; SD of depth: 5.544 m) was 0.913 m with offset adjustment alone and 0.648 m (0.265 m or 29.0% smaller) with the additional gain adjustment. This means that the additional gain adjustment improves not only the fitting for pixels with known depth but also the accuracy of predicted depths for other pixels. Thus, we can confidently recommend the use of predictor (9) (with the additional gain adjustment) rather than predictor (7) (with the offset adjustment alone).

The estimated coefficients of these predictors are listed in Table 3, for future use. To apply the coefficients of predictor (9) to water depth mapping of other images, the offset ($\beta_{0,n}$) and gain (p_n) need to be adjusted using a minimum of two pixels with known depth per image, as described in IV. Note that this minimum is much smaller than that required for the conventional estimation of all $M+1$ (e.g., 7 for WorldView-2) coefficients in (6) for each image. Naturally, the more pixels with known depth are used for the calibration, the better the prediction accuracy will be.

It should also be noted that the coefficients are usable even when no *in-situ* depth measurements are available. Obviously, predictor (7) (with the offset adjustment alone) can predict the relative depth in the same unit as h, even if $\beta_{0,n}$ is arbitrarily chosen, and predictor (9) (with the additional gain adjustment) can predict a variable linearly related to water depth, even if $\beta_{0,n}$ and p_n are arbitrarily chosen. These relative depth mappings, independent of *in-situ* measurements, may further expand the potential

application of the generalized coefficients presented in Table 3.

Because there are a wide variety of bottom surface and water quality types in the world, we cannot expect the coefficients presented in Table 3 to be accurately applicable to all locations. The conditions under which these coefficients yield sufficiently accurate bathymetry are not yet clear and require further investigation.

VI. CONCLUSION

To enable application of the multispectral water-depth predictor proposed by Lyzenga *et al.* (2006) using a minimal amount of *in-situ* data, we have estimated and presented two sets of generalized predictor coefficients. One set was estimated by fitting the predictor to pixels with known depth from six WorldView-2 images of coral reefs, using a recently proposed generalization technique (Kanno and Tanaka 2012). This technique adjusts the offset of the predictor for each image and thereby removes the effect of above-surface optical conditions on the other coefficients. The other set was estimated by applying an additional, and newly proposed, generalization technique, which adjusts the gain of the predictor for each image and thereby reduces the effect of in-water attenuation coefficients on the other coefficients. The fitting and the prediction accuracy were significantly better for the latter set. For example, for the six target images (SD of depth: 5.544 m), the RMSE of prediction, evaluated by cross validation, was 0.913 m using the first set and 0.648 m using the second set. Based on these results, we can confidently recommend use of the latter set of coefficients.

With the generalized predictor coefficients presented in this study, one can predict the water depth distribution from WorldView-2 imagery using a minimal number of *in-situ* depth measurements or perform relative depth mapping in the absence of *in-situ* data. This should significantly expand the applicability of Lyzenga's predictor and thereby increase the feasibility of remote bathymetry. Future

studies could investigate the conditions under which the proposed coefficients yield sufficiently accurate results by applying them to other images of shallow water areas.

ACKNOWLEDGMENT

This work was supported in part by a Grant-in-Aid for Research Activity Start-up (#22860044) from the Japan Society for the Promotion of Science. Depth measurements with a multi-narrow-beam echo sounder (Reson SeaBat 7125) were provided by the U.S. Naval Oceanographic Office via the website of the National Oceanic & Atmospheric Administration (NOAA)'s National Geophysical Data Center. Special thanks to Yukio Koibuchi of The University of Tokyo and Saki Nobuta and Kohei Ishida of Yamaguchi University, who helped with *in-situ* bathymetry.

REFERENCES

Bramante, J.F., D.K. Raju, and T.M. Sin. 2013. Multispectral derivation of bathymetry in Singapore's shallow, turbid waters. *International Journal of Remote Sensing* 34: 2070-2088.

Bryant, R.G., and D.J. Gilvear. 1999. Quantifying geomorphic and riparian land cover changes either side of a large flood event using airborne remote sensing: River Tay, Scotland. *Geomorphology* 29: 307-321.

Clark, R.K., T.H. Fay, and C.L. Walker. 1987. Bathymetry calculations with Landsat-4-TM imagery under a generalized ratio assumption. *Applied Optics* 26: 4036-4038.

Clark, R.K., T.H. Fay, and C.L. Walker. 1990. Shallow-water bathymetry models using multispectral digital data. *Journal of Imaging Technology* 16: 170-175.

Daniell, J.J. 2008. Development of a bathymetric grid for the Gulf of Papua and adjacent areas: A note describing its development. *Journal of Geophysical Research* 113: F01S15.

Feurer, D., J.S. Bailly, C. Puech, Y. Le Coarer, and A.A. Viau. 2008. Very-high-resolution mapping of river-immersed topography by remote sensing. *Progress in Physical Geography* 32: 403-419.

Flener, C., E. Lotsari, P. Alho, and J. Käyhkö. 2012. Comparison of empirical and theoretical remote sensing based bathymetry models in river environments. *River Research and Applications* 28: 118-133.

Gentle, J.E. 1998. *Numerical linear algebra for applications in statistics*, 166-167. New York: Springer-Verlag.

Hastie, T., R. Tibshirani, and J. Friedman. 2009. *The elements of statistical learning: Data mining, inference, and prediction. Second Edition*. Springer.

Hogrefe, K.R., D.J. Wright, and E.J. Hochberg. 2008. Derivation and integration of shallow-water bathymetry: Implications for coastal terrain modeling and subsequent analyses. *Marine Geodesy* 31: 299-317.

Kanno, A., and Y. Tanaka. 2012. Modified Lyzenga's method for estimating generalized coefficients of satellite-based predictor of shallow water depth. *IEEE Geoscience and Remote Sensing Letters* 9: 715-719.

Leckie, D.G., E. Cloney, C. Jay, and D. Paradine. 2005. Automated mapping of stream features with high-resolution multispectral imagery: An example of the capabilities. *Photogrammetric Engineering & Remote Sensing* 71: 145-155.

Lee, Z.P., K.L. Carder, C.D. Mobley, R.G. Steward, and J.S. Patch. 1999. Hyperspectral remote sensing for shallow waters: 2. Deriving bottom depths and water properties by optimization. *Applied Optics* 38: 3831-3843.

Lyzenga, D.R. 1985. Shallow-water bathymetry using combined LIDAR and passive multispectral scanner data. *International Journal of Remote Sensing* 6: 115-125.

Lyzenga, D.R., N.R. Malinas, and F.J. Tanis. 2006. Multispectral bathymetry using a simple physically based algorithm. *IEEE Transactions on Geoscience and Remote Sensing* 44: 2251-2259.

Mobley, C. D., et al., 2005. Interpretation of hyperspectral remote-sensing imagery by spectrum matching and look-up tables. *Applied Optics* 44: 3576-3592.

Nelder, J.A., and R. Mead. 1965. A simplex algorithm for function minimization. *Computer Journal* 7: 308–313.

Paredes, J.M., and R.E. Spero. 1983. Water depth mapping from passive remote-sensing data under a generalized ratio assumption. *Applied Optics* 22: 1134-1135.

Ribeiro, S.R.A., J.A.S. Centeno, and C.P. Krueger. 2008. An estimate of depth from a bathymetric survey and IKONOS II data by means of artificial neural network. *Boletim de Ciências Geodésicas* 14: 171-185.

Spitzer D., and R.W.J. Dirks. 1987. Bottom influence on the reflectance of the sea. *International Journal of Remote Sensing* 8: 279-290.

Stumpf, R.P., K. Holderied, and M. Sinclair. 2003. Determination of water depth with high-resolution satellite imagery over variable bottom types. *Limnology and Oceanography* 48: 547-556.

Su, H.B., H.X. Liu, and W.D. Heyman. 2008. Automated derivation of bathymetric information from multi-spectral satellite imagery using a non-linear inversion model. *Marine Geodesy* 31: 281-298.

Winterbottom, S.J., and D.J. Gilvear. 1997. Quantification of channel bed morphology in gravel-bed rivers using airborne multispectral imagery and aerial photography. *Regulated Rivers: Research & Management* 13: 489-499.

FIGURES AND TABLES WITH THEIR CAPTIONS

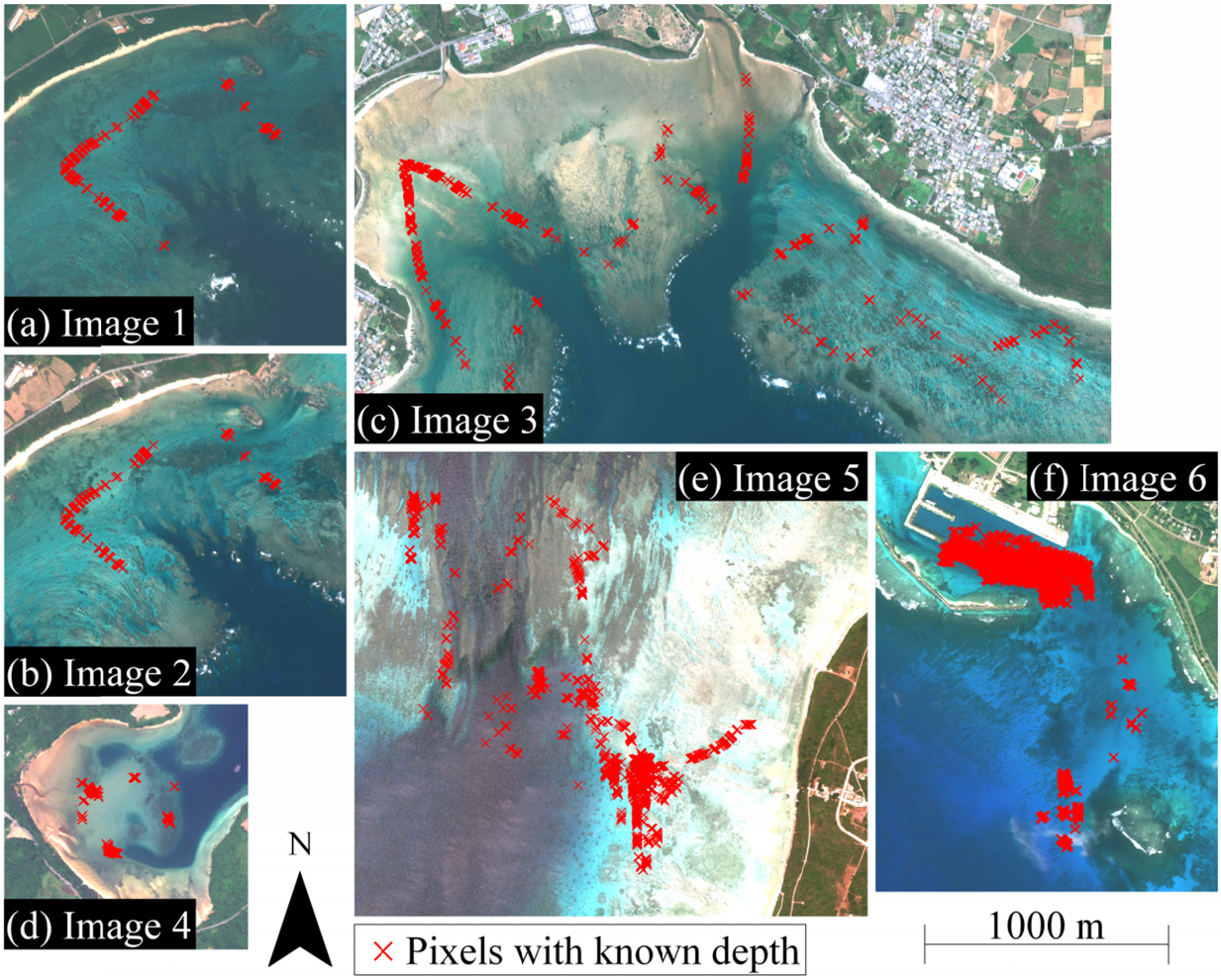

Fig. 1. True color composites of the WorldView-2 images used. Pixels with known depth are shown in red. The scale bar applies to all images. This figure includes copyrighted materials from DigitalGlobe, Inc. All Rights Reserved.

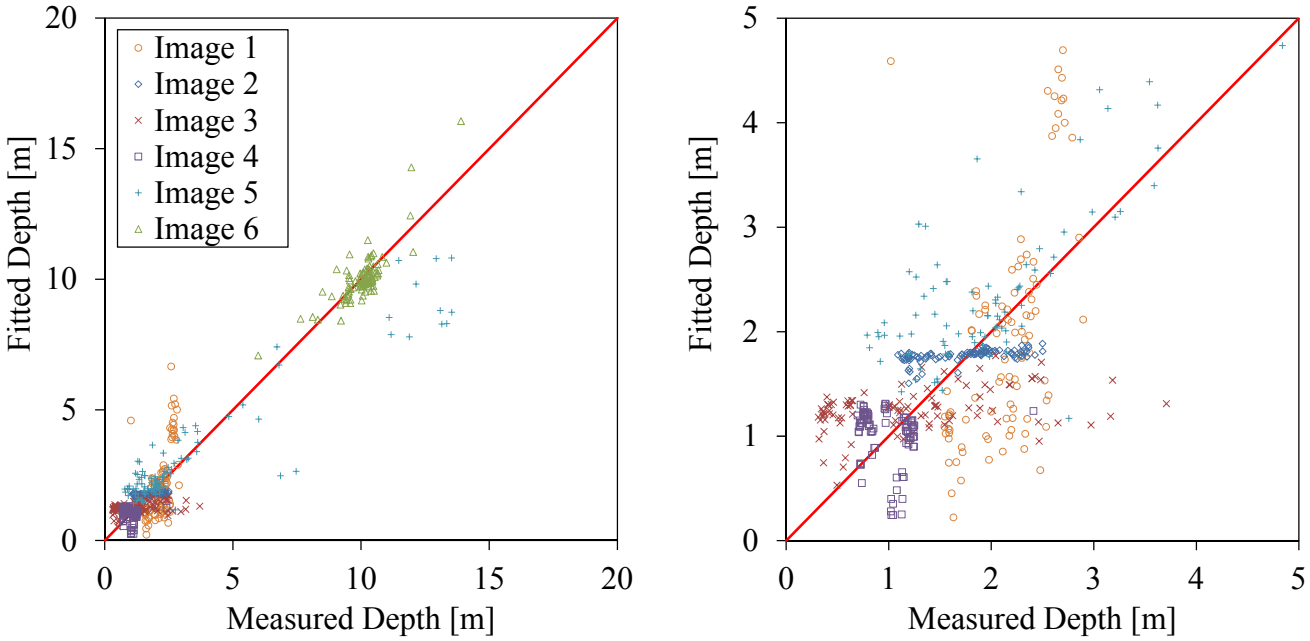

(a) Plot for the entire depth range

(b) Enlarged plot for depth range of 0–5 m

Fig. 2. Scattergram of fitted depth against measured depth for the fitting of (8) to the pixels with known depth from the six target images. For ease of viewing, only 100 randomly sampled pixels are plotted for each image. Because the pixels with known depth in images 1–4 are concentrated in the shallow domain, an enlarged plot for depth range 0–5 m (b) is shown in addition to the plot for the entire depth range (a).

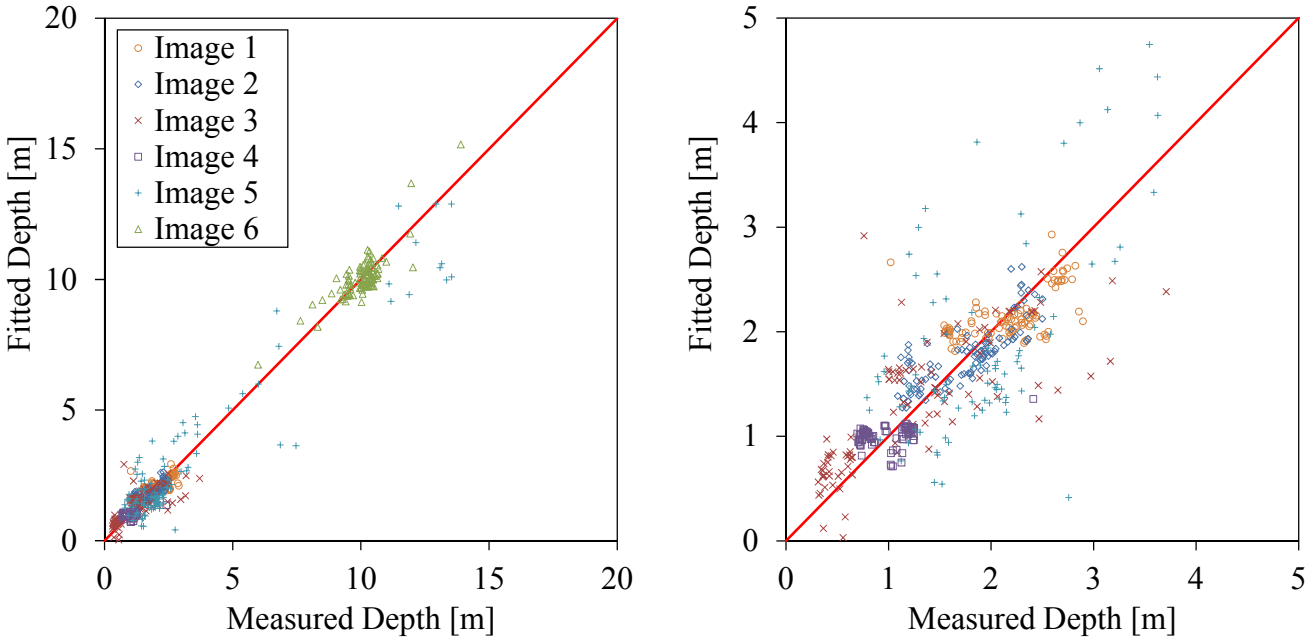

(a) Plot for the entire depth range

(b) Enlarged plot for depth range of 0–5 m

Fig. 3. Scattergram of fitted depth against measured depth for the fitting of (10) to pixels with known depth from the six target images. For ease of viewing, only 100 randomly sampled pixels are plotted for each image, and an enlarged plot for depth range 0–5 m (b) is shown in addition to the plot for the entire depth range (a).

Table 1. Specifications of target images and pixels with known depth. Here, θ_S is the solar zenith angle and θ_V is the nadir view angle below the water surface. The pixel size of WorldView-2 imagery is 2×2 m^2.

WorldView-2 image				Pixels with known depth		
Image ID	Location	Acquisition date	$\sec\theta_S + \sec\theta_V$	Number	Mean longitude [degrees]	Mean latitude [degrees]
1	Yaeyama islands, Japan	2010/3/24	2.130	160	124.276	24.484
2		2010/9/21	2.140	137	124.276	24.484
3		2010/9/21	2.181	637	124.210	24.348
4		2010/9/16	2.227	145	124.138	24.447
5		2011/8/24	2.034	869	124.072	24.334
6	Tinian island, U.S.	2009/12/7	2.224	4273	145.622	14.963

Table 2. Root Mean Square of Residuals (RMSR) of the fitting of the predictors to the training data and Root Mean Square Error (RMSE) of prediction evaluated by cross validation, for the application of the generalization techniques. Essential statistics for the pixels with known depth are also shown for reference.

Image ID	Pixels with known depth					RMSR (upper) and **RMSE** (lower) [m]		Decrease of RMSR (upper) and **RMSE** (lower) by additional gain adjustment	
	Number	Water depth [m]				Predictor (7) (with offset adjustment alone)	Predictor (9) (with offset and gain adjustment)	Absolute [m]	Relative [%]
		Min	Mean	Max	SD				
1	160	1.021	2.143	2.900	0.411	1.206 **1.233**	0.340 **0.343**	0.866 **0.890**	71.8 **72.2**
2	137	1.091	1.774	2.502	0.400	0.369 **0.373**	0.240 **0.245**	0.129 **0.129**	34.9 **34.4**
3	637	0.179	1.245	3.973	0.851	0.809 **0.807**	0.571 **0.573**	0.238 **0.234**	29.4 **29.0**
4	145	0.687	1.012	2.547	0.288	0.429 **0.432**	0.270 **0.283**	0.159 **0.149**	37.1 **34.6**
5	869	0.790	3.431	17.875	3.339	1.421 **1.437**	1.242 **1.253**	0.179 **0.184**	12.6 **12.8**
6	4273	4.563	10.013	15.363	1.157	0.647 **0.650**	0.593 **0.595**	0.054 **0.055**	8.3 **8.5**
Overall	6221	0.179	3.270*	17.875	5.544*	0.901* **0.913***	0.641* **0.648***	0.260** **0.265****	28.8** **29.0****

* Weighted values (the weighting is described in Section V.A.)

** Values derived from weighted values

Table 3. Estimated coefficients of the predictors (7) and (9). $\beta_i (i = 1, \cdots, 6)$ is the coefficient for band i of WorldView-2 imagery. The offset $\beta_{0,n}$ and the gain p_n (for predictor (9)) need to be estimated for each image to which these coefficients are applied.

Predictor	β_1	β_2	β_3	β_4	β_5	β_6
(7)	-0.475385	8.30074	-10.8218	-2.57621	0.313112	0.315611
(9)	-0.627429	37.2749	-67.2247	-14.8380	-0.295890	0.826530